

Structural phase transition and quasi-layered active-ion distribution suppress concentration quenching in Tb^{3+}-activated $KBi(MoO_4)_2$

Mengyu Zhang(张梦宇), Shujing Pan(潘淑晶), Haitang Hu(胡海棠), Wenzhi Su(宿文志), Yong Zou(邹勇), Shoujun Ding(丁守军), and Qingli Zhang(张庆礼)

Citation: Chin. Phys. B, 2026, 35 (**1**): 017801. DOI: 10.1088/1674-1056/ae1c25
http://cpb.iphy.ac.cn; http://iopscience.iop.org/cpb

What follows is a list of articles you may be interested in

Coupling between phonon and short-range spin correlations in frustrated spinel $LiFeCr_4O_8$

Xiang Li(李想), Wei Ren(任玮), Bo Zhang(张博), Yan-Zhen Cai(蔡焱桢), Zhi-Wei Li(李志伟), Jianting Ji(籍建葶), Feng Jin(金峰), Anmin Zhang(张安民), and Qingming Zhang(张清明)
Chin. Phys. B, 2025, 34 (**11**): 117801. DOI: 10.1088/1674-1056/ade4b4

Magnetic-field-induced photoluminescence enhancement in type-I quantum wells: A quantitative probe for interface flatness

Jun Shao(邵军), Man Wang(王嫚), Xiren Chen(陈熙仁), Liangqing Zhu(朱亮清), F. X. Zha(查访星), H. Zhao, Shumin Wang(王庶民), and Wei Lu(陆卫)
Chin. Phys. B, 2025, 34 (**10**): 107802. DOI: 10.1088/1674-1056/adf5a7

Temperature-dependent photoluminescence of lead-free cesium tin halide perovskite microplates

Jiayu Tan(谭佳雨), Yixuan Zhou(周译玄), De Lu(卢德), Xukun Feng(冯旭坤), Yuqi Liu(刘玉琪), Mengen Zhang(张蒙恩), Fangzhengyi Lu(卢方正一), Yuanyuan Huang(黄媛媛), and Xinlong Xu(徐新龙)
Chin. Phys. B, 2023, 32 (**11**): 117802. DOI: 10.1088/1674-1056/ad028e

Enhanced photoluminescence of monolayer MoS_2 on stepped gold structure

Yu-Chun Liu(刘玉春), Xin Tan(谭欣), Tian-Ci Shen(沈天赐), and Fu-Xing Gu(谷付星)
Chin. Phys. B, 2022, 31 (**8**): 087803. DOI: 10.1088/1674-1056/ac657b

Temperature-dependent Raman spectroscopic study of ferroelastic $K_2Sr(MoO_4)$

Ji Zhang(张季), De-Ming Zhang(张德明), Ran-Ran Zhang(张冉冉)
Chin. Phys. B, 2018, 27 (**11**): 117801. DOI: 10.1088/1674-1056/27/11/117801

RAPID COMMUNICATION

Structural phase transition and quasi-layered active-ion distribution suppress concentration quenching in Tb^{3+}-activated $KBi(MoO_4)_2$

Mengyu Zhang(张梦宇)[1,2,†], Shujing Pan(潘淑晶)[1,2,†], Haitang Hu(胡海棠)[3,4], Wenzhi Su(宿文志)[1,2], Yong Zou(邹勇)[1,2], Shoujun Ding(丁守军)[1,2,‡], and Qingli Zhang(张庆礼)[4]

[1] *School of Microelectronics and Data Science, Anhui University of Technology, Maanshan* 243002, *China*
[2] *Anhui Provincial Joint Key Laboratory of Disciplines for Industrial Big Data Analysis and Intelligent Decision, Maanshan* 243002, *China*
[3] *University of Science and Technology of China, Hefei* 230026, *China*
[4] *Anhui Institute of Optics and Fine Mechanics, Chinese Academy of Sciences, Hefei* 230031, *China*

(Received 14 September 2025; revised manuscript received 24 October 2025; accepted manuscript online 6 November 2025)

Conventional Tb^{3+}-doped phosphors typically suffer from concentration quenching once the doping level exceeds a critical threshold. Consequently, the development of Tb^{3+} phosphors with intrinsic resistance to concentration quenching has become a key research focus. In this work, we successfully synthesized $KBi(MoO_4)_2$: x%Tb^{3+} (x = 0–100 at%) (denoted as KBM: x%Tb^{3+}) phosphors via a high-temperature solid-state reaction. Remarkably, no concentration quenching was observed across the entire doping range. This anti-quenching behavior originates from the large Tb^{3+}–Tb^{3+} interionic distance (> 5 Å) inherent to the quasi-layered crystal structure, which effectively suppresses multipole-interaction-mediated energy migration. At full Tb^{3+} substitution (x = 100 at%), the material undergoes a structural phase transition from the monoclinic KBM phase to the triclinic α-$KTb(MoO_4)_2$ (α-KTM) phase. The α-KTM phosphor exhibits excellent thermal stability (activation energy = 0.6129 eV) and a single-exponential decay profile, whereas KBM: x%Tb^{3+} (x < 100%) display double-exponential decay behaviors, attributed to dual energy transfer pathways. These findings provide new insights into the luminescence mechanisms of high-concentration rare-earth-doped systems and offer guidance for designing next-generation anti-quenching phosphors.

Keywords: Tb^{3+} doping, layered crystal structure, anti-concentration quenching, structural phase transition

PACS: 78.55.–m, 87.15.mq, 32.50.+d, 33.50.–j

DOI: 10.1088/1674-1056/ae1c25 **CSTR:** 32038.14.CPB.ae1c25

1. Introduction

White light-emitting diodes (WLEDs) are among the most prominent solid-state lighting and display technologies due to their high efficiency, energy savings, environmental friendliness, and long operational lifetime.[1–5] The performance of phosphor-converted WLEDs is largely determined by the luminous efficiency, thermal stability, and spectral characteristics of the employed phosphor materials.[1,6] In recent years, the development of novel phosphors with outstanding overall performance has become a major research focus. Among various luminescent hosts, molybdate-based materials have attracted considerable attention due to their structural diversity, robust physicochemical stability, and relatively mild synthesis conditions.[7,8]

Terbium ions (Tb^{3+}) are widely recognized as an important green-emitting activator in WLEDs. Their intense, narrow-band green emission, originating from the characteristic $^5D_4 \rightarrow {}^7F_5$ transition, is essential for achieving a high color rendering index.[9–11] However, a common issue in conventional Tb^{3+}-doped phosphors is concentration quenching, where the emission intensity decreases upon exceeding a critical dopant concentration.[12,13] This behavior has been widely reported in various host matrices. For example, in oxide hosts such as Y_2O_3, the quenching concentration typically falls between 5 at% and 8 at%, primarily due to energy migration via dipole–dipole interactions.[14] Phosphate-based hosts often exhibit an even lower critical concentration, around 1 at%; in $LiMgPO_4$, for instance, Tb^{3+} doping beyond 1.5 at% leads to a pronounced drop in emission intensity.[15] Therefore, the development of Tb^{3+}-doped systems that resist concentration quenching and maintain high emission efficiency even at high or complete doping levels is of substantial scientific and practical importance.

$KBi(MoO_4)_2$ (abbreviated as KBM), a molybdate host with a layered crystal structure, offers a unique platform to investigate the doping behavior of Tb^{3+} ions.[16,17] In this work, we systematically explored the structural evolution, luminescence properties, and energy transfer mechanisms of Tb^{3+} in KBM across the full concentration range, from undoped (0 at%) to complete substitution of Bi^{3+} by Tb^{3+}

†These authors contributed equally to this work.
‡Corresponding author. E-mail: sjding@ahut.edu.cn

© 2026 Chinese Physical Society and IOP Publishing Ltd. All rights, including for text and data mining, AI training, and similar technologies, are reserved.

(100 at%, yielding $KTb(MoO_4)_2$, abbreviated as KTM). Remarkably, the KBM: xTb^{3+} system exhibits an anomalous anti-concentration quenching phenomenon: the luminescence intensity increases monotonically with Tb^{3+} content from 0% to 100%, and shows no conventional quenching plateau or decline. Detailed analysis reveals that this behavior arises from the unusually large Tb^{3+}–Tb^{3+} separation (>5 Å) afforded by the quasi-layered crystal structure, which effectively suppresses multipolar-interaction-mediated energy migration. At full Tb^{3+} substitution, the material undergoes a structural phase transition from the monoclinic KBM to the triclinic α-KTM, accompanied by a shift in luminescence mechanism. Furthermore, the system demonstrates excellent thermal and cycling stability.

2. Experimental details

2.1. Preparation of samples

The Tb^{3+}-doped $KBi(MoO_4)_2$ (KBM) samples were synthesized via a high-temperature solid-state reaction method. High-purity reagents, including K_2CO_3 (99.9%), Bi_2O_5 (99.99%), MoO_3 (99.9%), and Tb_2O_3 (99.9%) from Aladdin, were used as starting materials. The doping concentrations of Tb^{3+} ions in the KBM host were selected as 0 at%, 10 at%, 30 at%, 50 at%, 70 at%, and 100 at%. The raw materials were accurately weighed according to the stoichiometric ratio, then were mixed in an agate mortar and ground for 30 min. The thoroughly ground mixture was transferred into a crucible and placed in a muffle furnace. The temperature was gradually increased to 600 °C over a period of 4 hours and maintained at this temperature for 12 hours to ensure complete reaction. Afterward, the sample was cooled to room temperature. Finally, the synthesized samples were ground again for further characterization.

2.2. Characterizations

Phase structural analysis was performed using a Bruker D8 Advance x-ray diffractometer (XRD) equipped with Cu-$K\alpha$ radiation (wavelength $\lambda = 1.5406$ Å). Scanning was conducted in continuous mode over a 2θ angle range of 10°–80°, with a step size of 0.02°. The morphology and elemental distribution of the samples were characterized using a JSM-6510 scanning electron microscope (SEM). The excitation spectra, emission spectra and fluorescence decay curves were obtained using an Edinburgh FLSP-920 spectrometer, fitted with a xenon lamp as the excitation source. The temperature-dependent spectra were recorded by the same spectrometer equipped with a Lake Shore 355 temperature controller with a precision of ±0.5 K.

3. Results and discussion

3.1. Structure analysis

To comprehensively investigate the phase purity and structural characteristics of the samples, we performed x-ray diffraction (XRD) analysis followed by Rietveld refinement. Figure 1(a) displays the XRD patterns of Tb^{3+}-doped KBM samples with doping concentrations ranging from 0% to 70%. Since no standard reference pattern is available for KBM, the standard pattern of $RbBi(MoO_4)_2$ (RBM) (ICSD #4181) was adopted as a reference. This decision is based on the similarity in crystal structure and electronic configurations between K and Rb, both alkali metals in the same group of the periodic table. Consequently, the XRD pattern of RBM was employed for structural analysis and phase identification of KBM. The XRD results indicate that the patterns of x Tb^{3+}-doped KBM samples (KBM: xTb^{3+}) closely match the reference pattern, demonstrating that Tb^{3+} successfully substitutes for Bi^{3+} at the lattice sites within the KBM: xTb^{3+} system. Furthermore, the XRD patterns exhibit a significant angular shift in diffraction peaks as the Tb^{3+} doping concentration increases. This phenomenon can be attributed to the noticeable difference in ionic radii between Tb^{3+} and Bi^{3+}. The ionic radius of Tb^{3+} (CN = 8, $R = 1.04$ Å) is smaller than that of Bi^{3+} (CN = 8, $R = 1.17$ Å). According to Bragg's law, the substitution of the smaller Tb^{3+} ion reduces the interplanar spacing (d), resulting in an increased diffraction angle (2θ), and thus, a shift of the diffraction peaks toward higher angles.

Figure 1(b) shows the XRD pattern of KTM, which is formed by the complete substitution of Bi^{3+} with Tb^{3+} at 100% doping concentration. The XRD analysis reveals that the diffraction patterns of the synthesized KTM samples closely align with the α-KTM reference spectra in terms of peak positions and relative intensities. However, the patterns deviate significantly from both KBM and β-KTM, confirming a structural transformation at 100% Tb^{3+} doping. Specifically, the monoclinic KBM phase (space group $P21$) transitions to the triclinic α-KTM phase (space group $P1$) upon full substitution of Bi^{3+} by Tb^{3+}.[18,19]

Additionally, the Rietveld refinement of KBM: 10 at% Tb^{3+} (Fig. 1(c)) reveals that, at doping concentrations below 100%, the crystal structure of KBM remains unchanged and maintains its original monoclinic structure. Figure 1(d) presents the Raman spectra of KTM and KBM. Analysis of the Raman peaks reveals high consistency between the KTM and KBM samples in the middle- and high-frequency regions. However, in the low-frequency domain, the Raman peaks of KTM are predominantly centered at 137 cm^{-1}, 104 cm^{-1}, and 65 cm^{-1}, while those of KBM are located at 140 cm^{-1} and

75 cm^{-1}.[20,21] Since phonon energy (E) is directly proportional to vibrational frequency (ν) via the relation $E = h\nu$,[22] this comparison indicates that KTM exhibits lower phonon energies than KBM in the low-frequency region. This structural transformation may be attributed to lattice distortion, which occurs as the smaller Tb^{3+} ions replace the larger Bi^{3+} ions, causing a shift from the monoclinic to the triclinic phase, as depicted in Fig. 1(e).[23] Figure 1(f) presents the SEM and elemental mapping results of KBM: xTb^{3+}, demonstrating a homogeneous distribution of Tb^{3+} across the constituent elements (K, Bi, Mo, and O), confirming the uniform doping of Tb^{3+} within the KBM matrix.

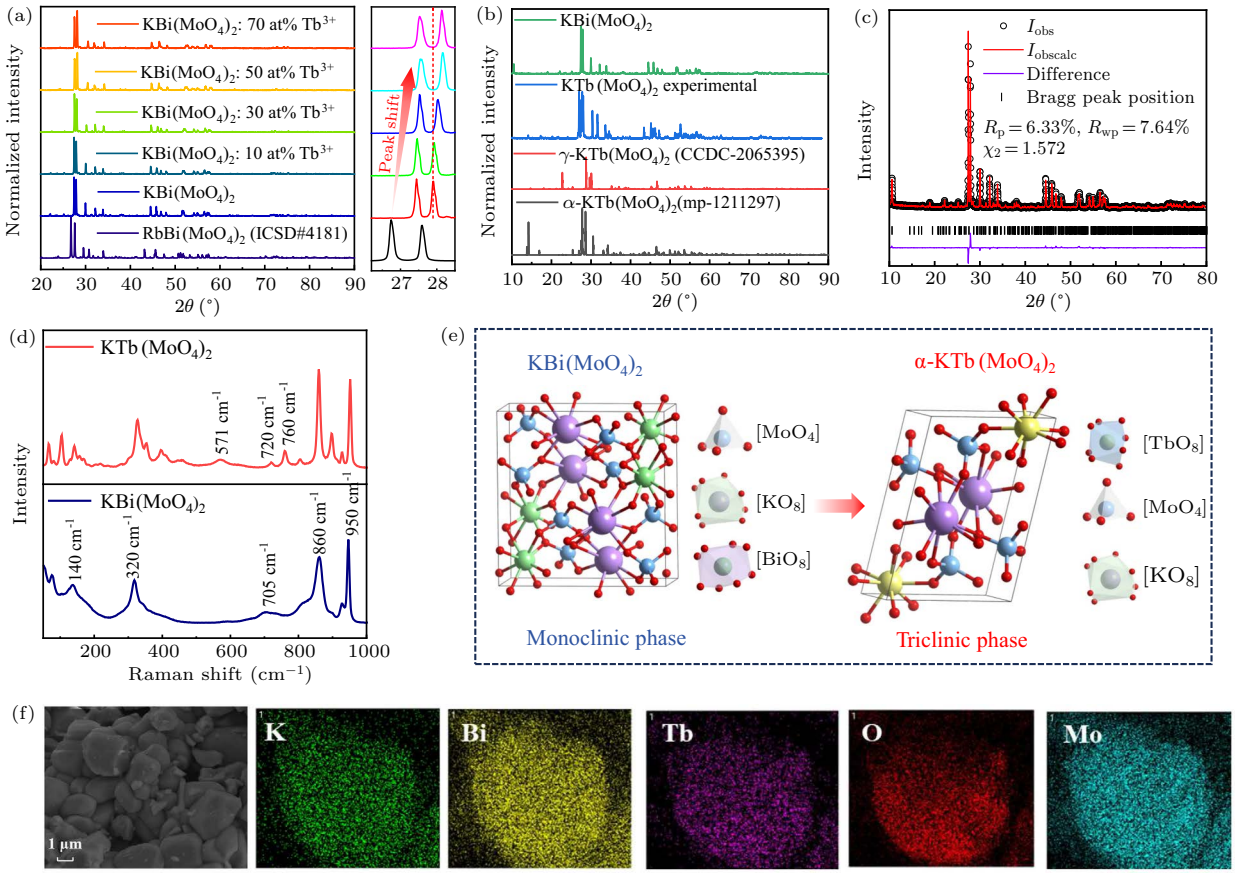


Fig. 1. (a) XRD patterns of KBM: xTb^{3+} (x = 0–70 at%), and the standard data of RBM phase (ICSD#4181). (b) XRD comparison of experimental KTM with KBM, α-KTM, and γ-KTM. (c) Rietveld refinement results of KBM: 10 at% Tb^{3+}. (d) Comparison of Raman peaks of KBM and KTM. (e) Structural transition diagram of KBM and α-KTM. (f) SEM image and element mapping of KBM: xTb^{3+}.

3.2. Luminescence properties

We measured the luminescence spectra of KTM and KBM: xTb^{3+} phosphors and systematically investigated their luminescence properties. Figure 2(a) illustrates the excitation spectra of the KTM phosphor at room temperature. At the monitoring wavelength of 550 nm, a broadband absorption spanning 280–330 nm with a maximum value at 308 nm is clearly observed, corresponding to the charge transfer band (CTB) of the $[MoO_4]^{2-}$ group.[24] In the 330–400 nm range, multiple excitation peaks were observed, which are attributed to the characteristic absorption transitions of Tb^{3+}. These peaks correspond to the characteristic wavelengths of 360 nm ($^7F_6 \rightarrow {}^5D_2$), 370 nm ($^7F_6 \rightarrow {}^5D_4$+$^5L_9$), 380 nm ($^7F_6 \rightarrow {}^5G_5$), 390 nm ($^7F_6 \rightarrow {}^5L_{10}$), and 398 nm ($^7F_6 \rightarrow {}^5G_6$+$^5D_3$), respectively.[25] We compared the excitation characteristics of KTM and KBM: 30 at% Tb^{3+} phosphors in the range of 260–360 nm, as shown in Fig. 2(b). Despite the differences in emission intensity at different excitation wavelengths, both KTM and KBM: 30 at% Tb^{3+} show a strong absorption response under 305 nm laser excitation. It is noteworthy that the excitation spectra of KBM: 30 at% Tb^{3+} contain characteristic absorption transitions of Bi^{3+} ions under weak crystal field ($^1S_0 \rightarrow {}^3P_1$) and $[MoO_4]^{2-}$ charge transfer transition, whose peaks are located at 280 nm and 320 nm, respectively.[26,27] Whereas KTM has only $[MoO_4]^{2-}$ charge transition absorption under 305 nm excitation.

To further analyze the photoluminescence properties of the KBM: 30 at% Tb^{3+} phosphor, Fig. 2(c) shows the normalized emission spectra under different excitation wavelengths. Excitation wavelengths of 280 nm, 305 nm, and 379 nm were selected, corresponding to spectral lines depicted in blue, orange, and green, respectively. The results indicate that the positions of the emission peaks remained largely unchanged across different excitation wavelengths. Within the range of 450–700 nm, the most prominent emission peaks

were observed at 480 nm, 545 nm, 580 nm, and 630 nm. These peaks correspond to the transitions from the $^5D_4$ energy level of Tb^{3+} ions to the $^7F_6$, $^7F_5$, $^7F_4$, and $^7F_3$ energy levels, respectively.[28] We investigated the emission behavior of KBM phosphors with varying Tb^{3+} doping concentrations ($x = 0$ at%, 10 at%, 30 at%, 50 at%, 70 at%, 100 at%) under 305 nm and 379 nm excitation, as shown in Figs. 2(d) and 2(e). The emission intensity increased monotonically with Tb^{3+} concentration, reaching a maximum at $x = 100$ at%. Characteristic emission peaks were observed in the 450–700 nm range, with dominant peaks at 480 nm, 545 nm, 580 nm, and 625 nm, along with weak peaks at 650 nm, 670 nm, and 680 nm. All peaks correspond to the characteristic $^5D_4 \rightarrow {}^7F_J$ ($J = 6, 5, 4, 3, 2, 1, 0$) transitions of Tb^{3+} ions.[25] In investigating the effect of Tb^{3+} doping concentration on emission intensity, we observed a distinctive phenomenon. As depicted in Fig. 2(f), the normalized emission intensity increases continuously as the Tb^{3+} concentration rises from 0 at% to 100 at%, irrespective of excitation at 305 nm. This contrasts with typical concentration quenching behavior reported for fluorescent materials, where luminescence intensity plateaus or declines beyond a critical dopant concentration due to inter-ionic energy transfer and non-radiative transitions.[29,30] Remarkably, our samples exhibit persistent emission enhancement across the entire doping range (0–100 at%) without evidence of concentration quenching. The underlying mechanisms for this anomalous behavior will be analyzed in the following contents.

The color coordinate diagram and CIE chromaticity coordinate serve as core parameters for evaluating phosphor luminescence characteristics. Figure 2(g) displays the CIE coordinates of KBM: xTb^{3+} phosphors under 305 nm excitation. Increasing Tb^{3+} doping concentration induces a progressive shift of the color coordinates toward the green region in the chromaticity diagram. The upper-right inset contrasts KTM samples under daylight versus 305 nm excitation, exhibiting distinct green emission under 305 nm excitation. Furthermore, comparison of emission spectra for KTM and KBM: 50 at% Tb^{3+} under both 305 nm and 379 nm excitation (Fig. 2(h)) reveals consistent spectral profiles and emission colors aligned with CIE analysis. All observed peaks correspond to characteristic Tb^{3+} transitions, which indicates the existence of an energy transfer process.

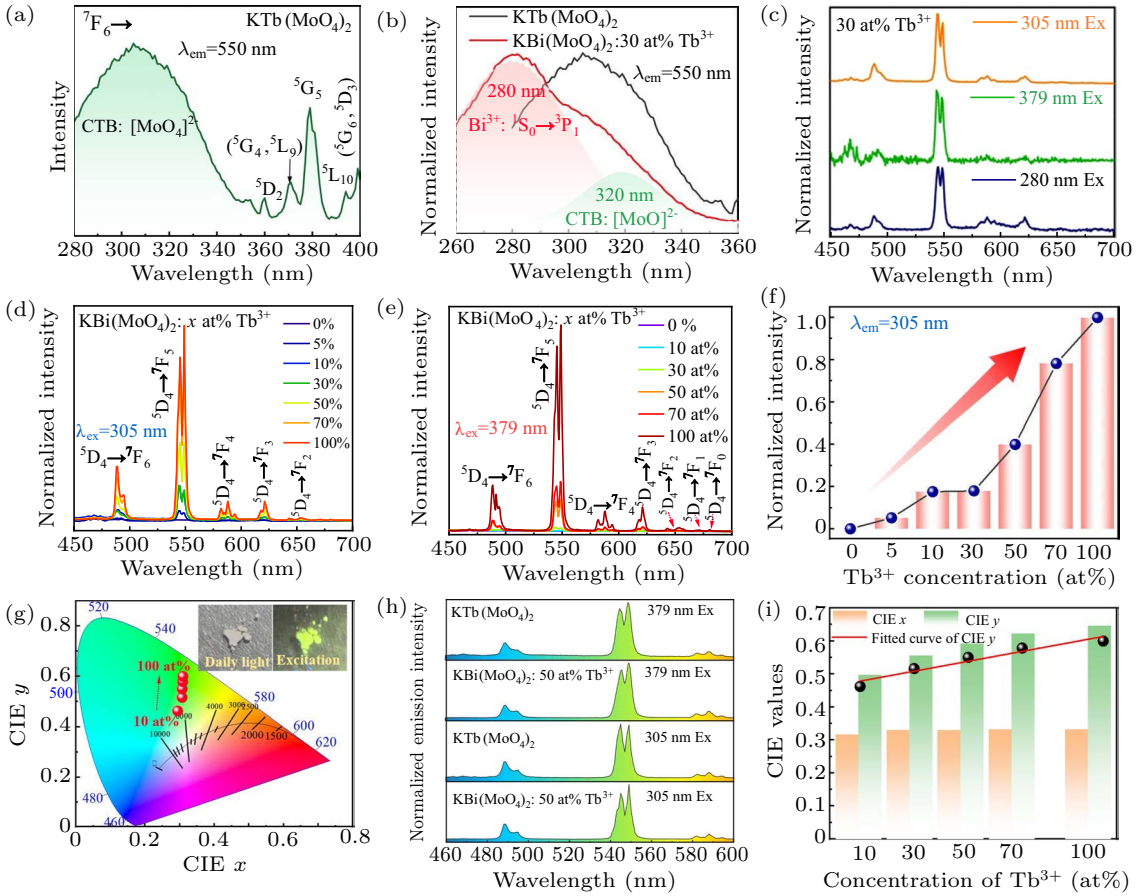


Fig. 2. (a) Excitation spectra of KTM phosphor in the range of 280–400 nm. (b) Excitation spectra of KTM and KBM: 30 at% Tb^{3+} phosphors in the range of 260–360 nm. (c) Emission spectra of KTM: 30 at% Tb^{3+} phosphor in the range of 450–700 nm under excitation at 280 nm, 305 nm and 379 nm. Emission spectra of KBM: xTb^{3+} phosphors in the range of 450–700 nm under 305 nm excitation (d) and 379 nm excitation (e). (f) Variation of emission intensity for different concentrations of Tb^{3+} under 305 nm excitation. (g) The CIE chromaticity coordinates with different Tb^{3+} doping concentrations ($x = 10$–100 at%). The inset displays images of KTM phosphor samples under daily light and 305 nm laser excitation, respectively. (h) Emission spectra of KTM and KBM: 50 at% Tb^{3+} under 305 nm and 379 nm excitation. (i) Linear correlation between CIE y-coordinate and Tb^{3+} doping concentration.

Additionally, as shown in Fig. 2(g), increasing Tb^{3+} doping concentration induces a systematic shift of color coordinates in the CIE chromaticity diagram from initial yellow-green toward the lime-green region. Although modest in magnitude, this shift exhibits excellent linearity. To quantify this trend, we performed linear fitting of the CIE y-coordinate, yielding the following equation:

$$y = 0.46323 + 0.0015x. \tag{1}$$

The fitting results reveal a strong linear correlation between Tb^{3+} concentration (x) and the CIE y-coordinate as shown in Fig. 2(i), with each concentration x uniquely determining both the y-value and corresponding emission color. This precise correspondence allows establishing a comprehensive CIE chromaticity database over the studied concentration range. Thus, for anti-counterfeiting applications, precisely designed concentration gradients can create high-dimensional security codes that exhibit continuous color gradients under UV illumination.

3.3. Anti-concentration quenching mechanism

To elucidate the intrinsic mechanism underlying the anti-concentration quenching phenomenon observed in doped samples, we conducted an in-depth investigation into their crystal structures and energy transfer. Generally, the concentration quenching phenomenon is closely associated with energy transfer between activator ions, where energy migrates from one activator ion to another and eventually reaches lattice defects or quenching centers.[6] This indicates that the absence of concentration quenching in KBM: $x$$Tb^{3+}$ materials may be attributed to inefficient energy transfer among Tb^{3+}–Tb^{3+} ions. As reported in Blasse's study,[31] exchange interactions dominate the energy transfer process when the ion spacing is below 5 Å, whereas multipolar interactions prevail when the spacing exceeds 5 Å. Notably, the contribution from multipolar interactions to energy transfer is significantly weaker than that from exchange interactions. As shown in Fig. 3(a), both monoclinic KBM and triclinic α-KTM exhibit layered crystal structures, where K^+ ions connect adjacent layers through ionic bonds. The large ionic radius of K^+ not only spatially separates Bi^{3+} and Tb^{3+} into different atomic layers but also significantly expands the interlayer spacing. This structural characteristic significantly increases the inter-ionic distance between activator ions. Based on the above structural characteristics, we calculated the Tb^{3+}–Tb^{3+} distances in KBM:10 at% Tb^{3+} and KTM using the following equations:[32]

$$R_0 = 2\left[\frac{3V}{4\pi X_c N}\right]^{1/3}, \tag{2}$$

where X_c denotes the critical concentration, N is the number of cations per unit cell, and V represents the unit cell volume. In the KBM: $x$$Tb^{3+}$ materials, the Tb^{3+}–Tb^{3+} distances were calculated for critical concentrations (X_c) of both 10 at% and 100 at%, given the absence of observable concentration quenching. For $X_c = 10\%$, substituting $V = 635.563$ Å^3 and $N = 4$ into the equation yields a Tb^{3+}–Tb^{3+} distance of 14 Å. At $X_c = 100\%$ (with $V = 662.015$ Å^3 and $N = 2$), the calculated distance decreases to 6 Å. These results demonstrate that the Tb^{3+}–Tb^{3+} separation remains above 5 Å even at the maximum doping concentration of 100 at%. According to energy transfer theory, multipolar interactions become dominant in this case, effectively suppressing both cross-relaxation and resonance energy transfer processes, thereby significantly reducing the probability of concentration quenching.[31] Meanwhile, the absence of concentration quenching is linked to the distinctive electronic structure of Tb^{3+} ions. The 4f electron orbitals are effectively shielded by the outer $5s^25p^6$ electron shells, which dramatically weakens their interaction with neighboring ions or lattice defects.[33] This shielding effect consequently suppresses nonradiative transitions that would otherwise lead to concentration quenching. Thus, this shielding effect suppresses the occurrence of non-radiative transitions, consequently giving rise to the phenomenon of anti-concentration quenching. Furthermore, the substantial energy gap between Tb^{3+} ground state ($^7F_6$) and excited state ($^5D_4$) not only reduces energy transfer probability but also markedly weakens electron–phonon coupling, thereby further suppressing the concentration quenching mechanism.[33]

The emission spectra of the undoped and low-Tb^{3+}-doped (< 15%) samples, together with the KTM sample, are shown in Fig. 3(b). It is evident that the undoped sample exhibits a pronounced broadband emission near 470 nm (in clear contrast to the Bi^{3+}-free KTM sample), which is assigned to the intrinsic Bi^{3+} $^3P_1 \rightarrow {}^1S$ transition. Notably, the intrinsic Bi^{3+} emission progressively weakens with increasing Tb^{3+} concentration, indicating resonant energy transfer between Bi^{3+} and Tb^{3+}; the proposed transfer mechanism is depicted in Fig. 3(c). At low doping concentrations ($x < 100$ at%), energy transfer from both Bi^{3+} ($^1S \rightarrow {}^3P_1$ under 280 nm excitation) and $[MoO_4]^{2-}$ ($^1A_1 \rightarrow {}^1T_2$ under 305 nm excitation) sensitizes the $^5D_3$ level of Tb^{3+}. Concurrently, Tb^{3+} directly absorbs 379 nm photons (via $^7F_6 \rightarrow {}^5D_3$ transition).[34–36] Subsequently, electrons in the $^5D_3$ level undergo non-radiative relaxation to the $^5D_4$ level. Ultimately, the $^5D_4$ excited electrons transition to the ground states ($^7F_6 \rightarrow {}^7F$), activating characteristic Tb^{3+} emissions through radiative transitions that produce distinct wavelength bands and corresponding colors. At 100 at% Tb^{3+} doping concentration, complete replacement of Bi^{3+} sites by Tb^{3+} shifts the luminescence mechanism to a $[MoO_4]^{2-}$-Tb^{3+} synergistic system. Here, $[MoO_4]^{2-}$-mediated energy transfer (following UV absorption) cooperates with direct Tb^{3+} excitation to jointly drive the characteristic emissions. This concentration-dependent mechanism transition provides a fundamental basis for designing multimodal anti-counterfeiting materials.

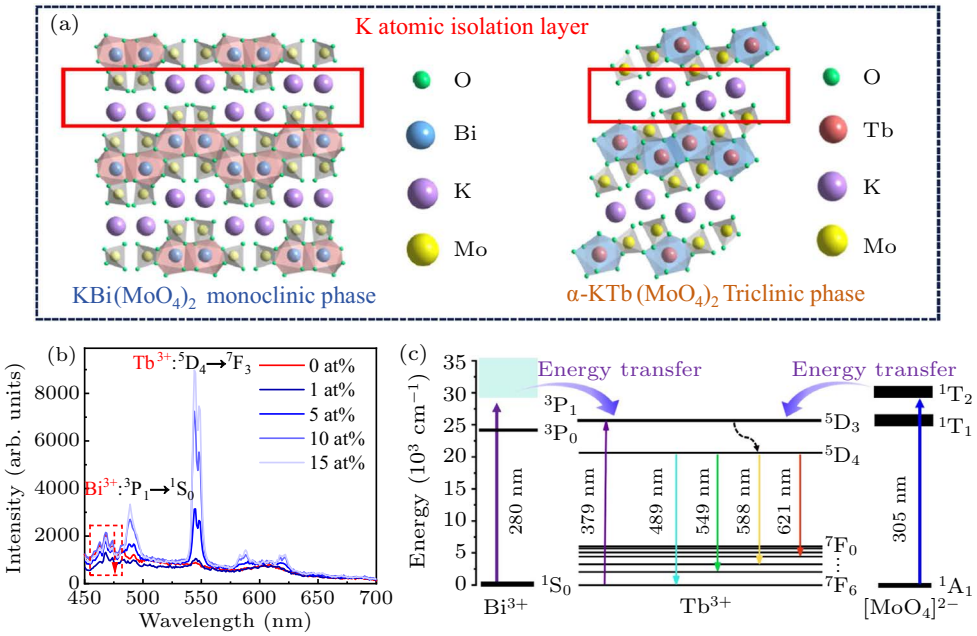


Fig. 3. (a) Crystal structure schematics of monoclinic KBM and triclinic α-KTM layered materials. (b) The emission spectra of the undoped and low-Tb^{3+}-doped (< 15%) samples, together with the KTM sample. (c) Energy transfer mechanism in the KBM: xTb^{3+}.

3.4. Luminescence thermal stability

To further investigate the properties of the phosphor samples, we compared the temperature-dependent luminescence of KBM: 50 at% Tb^{3+} and KTM over the range of 300 K to 440 K, as shown in Fig. 4(a). The luminescence intensity of both KBM: 50 at% Tb^{3+} and KTM gradually decreases as temperature increases, a behavior that manifests characteristic thermal quenching. The thermal quenching mechanism can be primarily attributed to enhanced lattice vibrations at elevated temperatures, which induce the formation of Urbach tail states through the tail of electronic state distribution from the conduction band edge into the bandgap.[37] These tail states effectively overlap with the excited energy levels ($^5D_4$ and $^5D_3$) of Tb^{3+} ions, providing a nonradiative relaxation pathway where excited electrons can transition to the conduction band rather than returning to the ground state through radiative emission. In the low-frequency range, KBM: xTb^{3+} exhibits higher phonon energy than KTM at doping concentrations below 100%. This energy difference reduces the thermal quenching effect, which leads to a more gradual intensity decay, due to the fact that higher phonon energies may accelerate the non-radiative relaxation by promoting phonon–electron coupling, thus exacerbating the thermal quenching.[38] Furthermore, we examined the 2D temperature-dependent emission spectra of KBM: 50 at% Tb^{3+} and KTM under 379 nm excitation (Fig. 4(b)). Similar to the 305 nm excitation case, the characteristic Tb^{3+} emission peaks are observed, and their positions show no significant temperature shift. This further demonstrates that the crystal-field environment around Tb^{3+} in the host remains stable.

To deeply investigate the thermal stability of KTM and KBM: 50 at% Tb^{3+}, we performed thermal cycling tests on both phosphors (Fig. 4(c)). Under 379 nm excitation, the temperature underwent five complete cycles, each consisting of heating from 300 K to 440 K followed by cooling back to 300 K. To facilitate direct comparison of cycling stability, the luminescence intensity was normalized, as shown in Fig. 4(d). The results demonstrate that both materials exhibit excellent stability and repeatability.

The luminescence thermal stability discrepancy between KBM: 50 at% Tb^{3+} and KTM was quantitatively characterized by normalizing their temperature-dependent luminescence intensities over the 300–440 K range (Figs. 4(e) and 4(f)). Experimental data reveal that while both materials exhibit typical thermal quenching behavior, KTM demonstrates notably superior luminescence thermal stability compared to KBM: 50 at% Tb^{3+} under both 305 nm and 379 nm excitation. Specifically, KTM retains 63.2% of its initial luminescence intensity at 360 K under 305 nm excitation. This divergence stems from distinct local environments of Tb^{3+} ions: in the KTM host, Tb^{3+} occupies intrinsic lattice sites with optimal charge matching to host cations, establishing a uniform crystal field.[39] This configuration minimizes high-temperature lattice distortion and mitigates perturbation of Tb^{3+} excited states. By contrast, in the KBM: 50 at% Tb^{3+} system, Tb^{3+} substitutes for Bi^{3+} as a dopant ion. The significant ionic radius difference between Bi^{3+} and Tb^{3+} triggers lattice distortion, leading to inhomogeneous crystal field distribution around Tb^{3+}. As temperature increases, thermal vibrations amplify this distortion, promoting coupling between Tb^{3+} excited states and phonons. This enhances non-radiative transition rates, ultimately manifesting as accelerated luminescence decay.[40]

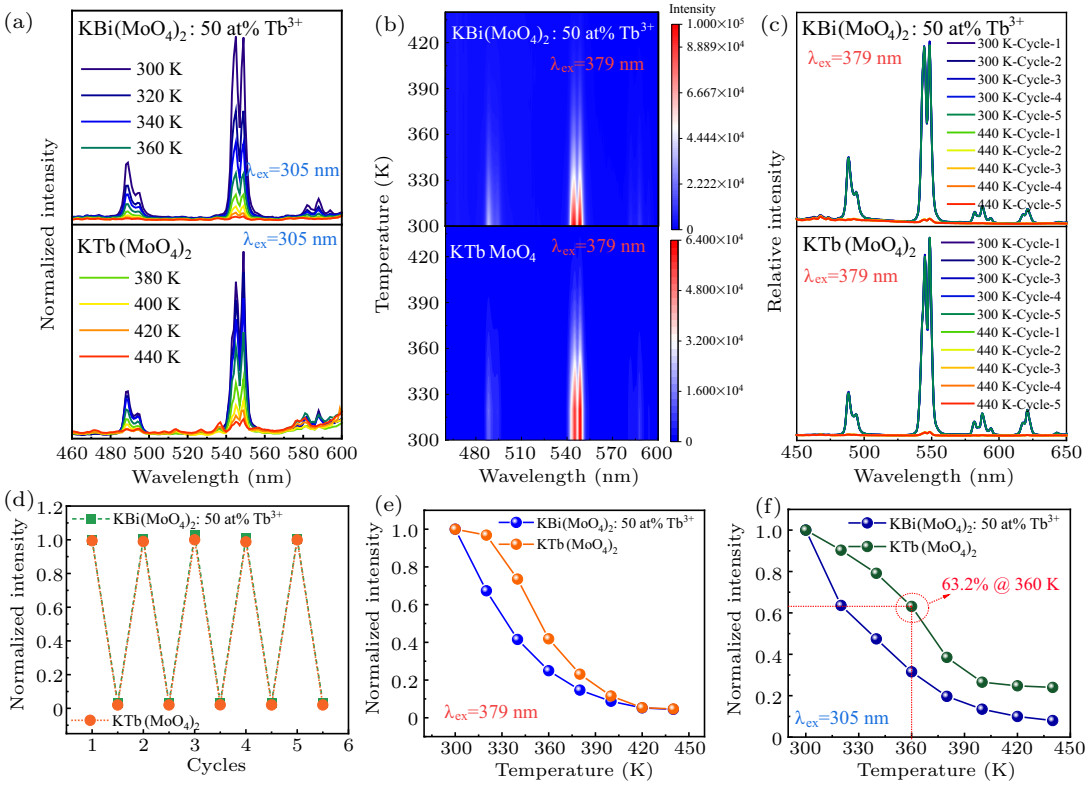


Fig. 4. Temperature-dependent emission spectra of KBM: 50 at% Tb^{3+} and KTM under (a) 305 nm excitation and (b) 379 nm excitation. (c) Relative intensity of KBM: 50 at% Tb^{3+} and KTM to five cycles of alternating temperatures between 300 K and 440 K. (d) Cycle measurement results of KBM: 50 at% Tb^{3+} and KTM under temperature alternating between 300 K and 440 K. Normalized photoluminescence intensity as a function of temperature for KBM: 50 at% Tb^{3+} and KTM under (e) 305 nm excitation and (f) 379 nm excitation.

3.5. Fluorescence decay properties

To further investigate the thermal stability properties of the phosphors, we applied the Arrhenius equation to determine activation energies and analyze their thermal quenching behaviors:[41]

$$I(T) = \frac{I_0}{1 + A\,e^{\frac{-E_a}{kT}}}, \tag{3}$$

where I_0 and $I(T)$ are the initial and temperature-dependent emission intensities, respectively. E_a refers to the thermal quenching activation energy, A is a constant, and k is the Boltzmann constant (8.62×10^{-5} eV/K). Figure 5(a) presents the thermal quenching activation energies E_a of KBM: 50 at% Tb^{3+} (0.4059 eV) and KTM (0.6129 eV). KTM exhibits a significantly higher activation energy than KBM: 50 at% Tb^{3+}, consistent with the conclusion of temperature-dependent luminescence characteristics of both phosphor materials in the preceding section. Notably, both phosphors exhibit substantially higher E_a than typical Tb^{3+}-doped materials, as shown in Table 1, confirming their exceptional thermal stability.

To delve deeper into the luminescence mechanism of the phosphors, we systematically investigated the fluorescence decay lifetimes of KBM: xTb^{3+} (x = 10 at%, 30 at%, 50 at%, 70 at% and 100 at%) phosphors with varying Tb^{3+} doping concentrations, as presented in Figs. 5(b) and 5(c). Notably, the fluorescence decay curve of the KTM sample follows a single-exponential decay model, yielding a fluorescence decay lifetime of 0.529 ms after fitting.[46] This behavior indicates that only one luminescence center for Tb^{3+} exists in the KTM host. However, KBM: xTb^{3+} (x = 10 at%, 30 at%, 50 at% and 70 at%) whose fluorescence decay was fitted with a double-exponential function[47]

$$I(t) = A_1 \exp(-t/\tau_1) + A_2 \exp(-t/\tau_2), \tag{4}$$

where components τ_1 (fast decay) and τ_2 (slow decay) demonstrate concentration-dependent evolution. As the doping concentration of Tb^{3+} increases from 10 at% to 70 at%, the value of τ_1 increases from 0.013 ms to 0.103 ms, and the value of τ_2 increases from 0.383 ms to 0.467 ms. These distinct fluorescence lifetime decay behaviors are closely related to their crystal structures and energy transfer mechanisms, as shown in Fig. 5(d). In KTM host, Tb^{3+} ions occupied intrinsic lattice sites within a uniform crystal field distribution. The $[MoO_4]^{2-}$ groups absorb energy and efficiently transfer it to adjacent

Table 1. Comparison of activation energies (E_a) of different doped Tb^{3+}-doped materials.

Phosphors	E_a (eV)	Ref.
KTM	0.6129	this work
KBM: 50 at% Tb^{3+}	0.4059	
$SrSO_4$: Tb^{3+}, Dy^{3+}	0.5	[42]
$YAl_3(BO_3)_4$: Tb^{3+}	0.585	[43]
α-$Sr_2P_2O_7$: Tb^{3+}	0.57	[44]
$YGdBO_3$: Tb^{3+}, Eu^{3+}	0.4	[45]

Tb^{3+} ions via a singular pathway. On the other hand, KBM: $x$$Tb^{3+}$ manifests dual luminescent centers of Bi^{3+} and Tb^{3+}. In addition, the doping of Tb^{3+} leads to lattice distortion and inhomogeneous crystal field distribution, which complicates the energy transfer paths. Specifically, the energy absorbed by Bi^{3+} ions is then transferred to Tb^{3+} via the ET-1 path, and the energy absorbed by $[MoO_4]^{2-}$ groups is transferred to Tb^{3+} via the ET-2 path. In summary, the differences in host structures lead to divergent luminescent behaviors: the KTM host has only one luminescent center and the KBM: Tb^{3+} hosts have dual centers. These structural distinctions directly manifest as single exponential versus double-exponential fluorescence decay behaviors, elucidating fundamental mechanistic divergences between these phosphors.

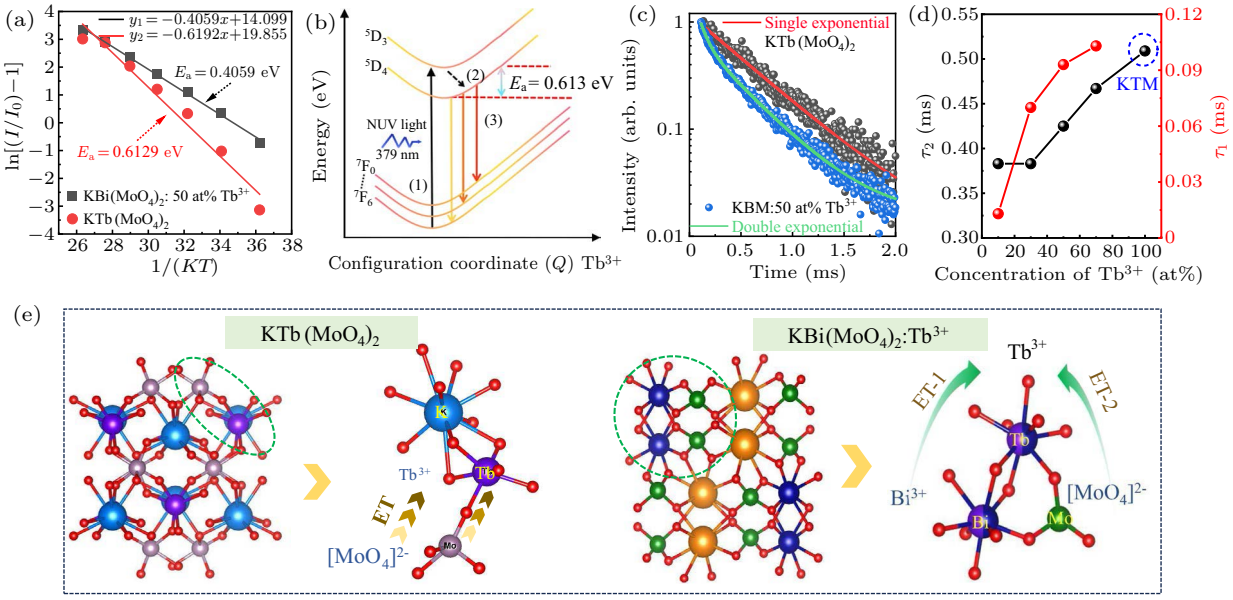


Fig. 5. (a) $\mathrm{Ln}\,[(I_0/I)-1]$ versus $1/(KT)$ plot of KBM: 50 at% Tb^{3+} and KTM phosphors. (b) Configurational coordinate schematic. (c) Fluorescence decay curves for the KTM phosphor. (d) Fluorescence decay times for the KBM: $x$$Tb^{3+}$ (x = 10 at%, 30 at%, 50 at% and 70 at%) and KTM phosphors. (e) Schematic illustration of energy transfer mechanisms in KTM and KBM: Tb^{3+}.

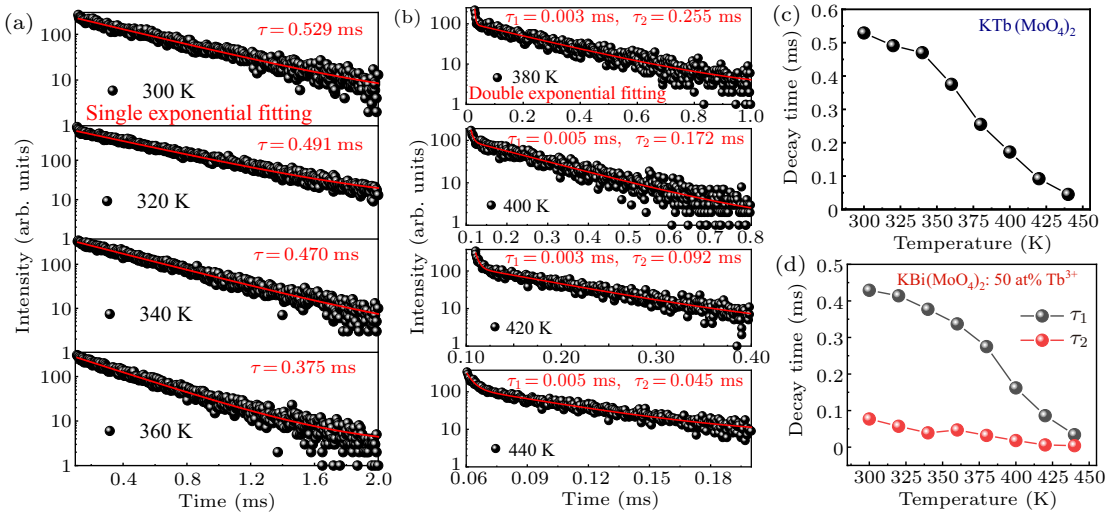


Fig. 6. (a)–(b) Fluorescence decay curves of KTM phosphor at different temperatures. (c) Fitted decay times at different temperatures of KTM phosphor. (d) Fitting fast decay (τ_1) and slow decay (τ_2) times at different temperatures of KBM: 50 at% Tb^{3+} phosphor.

To elucidate the temperature-dependent luminescence characteristics of the phosphors, the fluorescence lifetimes of KTM and KBM: 50 at% Tb^{3+} phosphors were probed across distinct temperature ranges. Figures 6(a) and 6(b) depict the fluorescence decay curves of KTM samples within the temperature intervals of 300–360 K and 380–440 K, respectively. Fitting analysis reveals that within the 300–360 K range, the fluorescence lifetime of KTM undergoes a gradual transition from 0.529 ms to 0.375 ms, and the decay behavior is amenable to single exponential function fitting. As the temperature increases to the 380–440 K range, the fluorescence decay manifests a double-exponential feature. This single exponential to double-exponential decay mode shift can be attributed to thermally-induced lattice distortion. The high temperature in-

tensifies the lattice thermal vibration, which changes the crystal field environment of some Tb^{3+} ions and splits the excited state energy levels, resulting in some ions being in a strongly coupled environment and others in a weakly coupled environment.[39] When the temperature reaches 380 K, the phonon–electron coupling is significantly enhanced, which activates the non-radiative transition channels and leads to phonon-assisted energy transfer between ions. Ultimately, this culminates in the fluorescence decay behavior evolving from single exponential to double exponentials. We systematically studied the temperature-dependent fluorescence lifetime properties of KBM: 50 at% Tb^{3+} and KTM phosphors as shown in Figs. 6(c) and 6(d). The experimental results demonstrate that between 300 K and 440 K, KBM: 50 at% Tb^{3+} consistently displays double-exponential fluorescence decay behavior. The fast decay component τ_1 represents the energy transfer from Bi^{3+} to Tb^{3+}, while the slow decay component τ_2 corresponds to direct excitation from $[MoO_4]^{2-}$ to Tb^{3+}.[20,27,33] Both lifetime components decrease with rising temperature. Specifically, τ_1 reduces from 0.429 ms to 0.034 ms, suggesting the energy transfer efficiency between Bi^{3+} and Tb^{3+} declines due to stronger lattice vibrations. Meanwhile, τ_2 shortens from 0.077 ms to 0.004 ms, mainly caused by enhanced multiphonon non-radiative relaxation at elevated temperatures. In comparison, KTM exhibits single-exponential decay characteristics, indicating it contains only one luminescent center.

4. Conclusion

In this work, KBM: Tb^{3+} phosphors were synthesized via high-temperature solid-state reaction, with their luminescence properties systematically characterized across a wide doping range (0–100 at% Tb^{3+}). Remarkably, these materials demonstrate an unusual anti-concentration quenching effect, where luminescence intensity increases monotonically with Tb^{3+} concentration. This distinctive behavior originates from the large interionic distances (>5 Å) between Tb^{3+} ions in the layered crystal structure, which effectively suppresses energy migration through multipole interactions. Complete substitution of Bi^{3+} with Tb^{3+} (100 at%) induces a structural phase transition from monoclinic to triclinic (α-KTM), exhibiting superior thermal stability (activation energy $= 0.6129$ eV). Precise control of Tb^{3+} doping concentration enables linear tuning of CIE chromaticity coordinates, suggesting potential applications in anti-counterfeiting technologies. Fluorescence lifetime analysis reveals mono-exponential decay for α-KTM, contrasting with the bi-exponential behavior observed at intermediate doping levels. These findings provide valuable insights for developing advanced rare-earth doped phosphors with applications in solid-state lighting and security marking.

Acknowledgements

This work was supported by the Natural Science Research Project of Anhui Province Education Department for Excellent Young Scholars (Grant No. 2024AH030007) and the National Natural Science Foundation of China (Grant No. 52202001).

References

[1] Cho J, Park J H, Kim J K and Schubert E F 2017 *Laser & Photonics Reviews* **11** 1600147
[2] Weinold M P, Kolesnikov S and Anadón L D 2025 *Nat. Energy* **10** 616
[3] Tian H, Liu J W, Qiu K, Song J and Wang D J 2012 *Chin. Phys. B* **21** 098504
[4] Li C, Zhang M, Zhang C, Su W, Zou Y, Ding S and Zhang Q 2025 *Chin. Phys. B* **34** 087502
[5] Zhang Q, Wang X, Wu Z, Li X, Zhang K, Song Y, Fan J, Wang C K and Lin L 2023 *Chin. Phys. B* **32** 103301
[6] Li G H, Yang N, Zhang J, Si J Y, Wang Z L, Cai G M and Wang X J 2020 *Inorg. Chem.* **59** 3894
[7] George S D B, Nirathintavida Nittakaran S, Arockiasamy J J, Madamala S, Narasimman L, Kuppamuthu S and Xavier S S 2025 *ACS Appl. Opt. Mater.* **3** 1011
[8] Yan L, Xing M, Ma Y, Kang L, Fu Y, Pang Q, Xin F, Wang H, Luo X and Tian Y 2024 *Spectrochimica Acta Part A: Molecular and Biomolecular Spectroscopy* **308** 123751
[9] Zeng C, Hu Y, Xia Z and Huang H 2015 *RSC Adv.* **5** 68099
[10] Tikale R V, Kadam A R, Michalska-Domańska M and Dhoble S J 2025 *Sci. Rep.* **15** 27748
[11] Fang L, Zhou X, Zhao Z, Zheng B, Xia H, Wang J, Song H and Chen B 2022 *Chin. Phys. B* **31** 127802
[12] Baby B, Thomas S, Jose J, Gopinath M, Biju P R and Joseph C 2025 *Journal of Luminescence* **277** 120895
[13] Dang P, Li G, Yun X, Zhang Q, Liu D, Lian H, Shang M and Lin J 2021 *Light Sci. Appl.* **10** 29
[14] Muenchausen R E, Jacobsohn L G, Bennett B L, McKigney E A, Smith J F, Valdez J A and Cooke D W 2007 *Journal of Luminescence* **126** 838
[15] Shi M, Zhang D and Chang C 2015 *J. Alloys Compd.* **627** 25
[16] Kang T W, Jeong G J, Kim J H, Bae B and Kim S W 2022 *New J. Chem.* **46** 10722
[17] Samal S K, Pushpendra, Yadav J and Naidu B S 2023 *Ceramics International* **49** 20051
[18] Morozov V A, Posokhova S M, Istomin S Ya, Deyneko D V, Savina A A, Redkin B S, Lyskov N V, Spassky D A, Belik A A and Lazoryak B I 2021 *Inorg. Chem.* **60** 9471
[19] Raj C J, Krishnan S, Dinakaran S, Priya S M N, Uthrakumar R and Das S J 2008 *Crystal Growth & Design* **8** 3956
[20] Wang M, Wang C, Wang J, Lu L, Gong X, Tang X, Zhang F and You J 2020 *Materials* **13** 5453
[21] Jayaraman A, Sharma S K, Wang S Y, Shieh S R, Ming L C and Cheong S W 1996 *Pramana J. Phys.* **47** 151
[22] Noras J M 1980 *J. Phys. C: Solid State Phys.* **13** 4779
[23] Zhou Y J, Zhang Y, Wang F J and Chen G L 2008 *Appl. Phys. Lett.* **92** 241917
[24] Wang H, Yang T, Feng L, Ning Z, Liu M, Lai X, Gao D and Bi J 2018 *J. Electron. Mater.* **47** 6494
[25] Demesh M, Gorbachenya K, Kisel V, Volkova E, Maltsev V, Koporulina E, Dunina E, Kornienko A, Fomicheva L and Kuleshov N 2021 *OSA Continuum* **4** 822
[26] Huang Y, Zhou L, Yang L and Tang Z 2011 *Opt. Mater.* **33** 777
[27] Ju H, Deng W, Wang B, Liu J, Tao X and Xu S 2012 *J. Alloys Compd.* **516** 153
[28] Joubert M F, Jacquier B and Moncorgé R 1983 *Phys. Rev. B* **28** 3725
[29] Shi M, Zhang D and Chang C 2015 *J. Alloys Compd.* **627** 25
[30] Boruc Z, Fetlinski B, Kaczkan M, Turczynski S, Pawlak D and Malinowski M 2012 *J. Alloys Compd.* **532** 92
[31] Lv Q, Shao B, Ma X, Yang S, Wang C, Dong Y, Dong E and Wang C 2023 *Spectrochimica Acta Part A: Molecular and Biomolecular Spectroscopy* **287** 122126

[32] Tingming Jiang T J, Xue Yu X Y, Xuhui Xu X X, Hongling Yu H Y, Dacheng Zhou D Z and Jianbei Qiu J Q 2014 *Chin. Opt. Lett.* **12** 011601
[33] Wang S, Lyu Z, Lu Z, Wang L, Wang J, Sun D, Tan T, Shen S and You H 2023 *J. Mater. Chem. C* **11** 10634
[34] Chi F, Liu Q, Zhang J, Jiang B, Niu X and Liu S 2023 *Opt. Mater.* **143** 114245
[35] Tsai Y Y, Chen H L, Chai Y L and Chang Y S 2013 *Opt. Mater.* **35** 317
[36] Wu X, Qin S, Zhang R, Guo Y and Huang J 2024 *ACS Appl. Nano Mater.* **7** 19593
[37] Jamal M U, Nagirnyi V, Chernenko K, Kotlov A, Smortsova Y and Spassky D 2025 *Materials Research Bulletin* **191** 113553
[38] Hwang T Y, Choi Y, Song Y, Eom N S A, Kim S, Cho H B, Myung N V and Choa Y H 2018 *J. Mater. Chem. C* **6** 972
[39] Mansouri S, Jandl S, Balli M, Laverdière J, Fournier P and Dimitrov D Z 2016 *Phys. Rev. B* **94** 115109
[40] Lin C C, Tsai T, Johnston H E, Fang H, Yu F, Zhou W, Whitfield P, Li Y, Wang J, Liu S and Attfield J P 2017 *J. Am. Chem. Soc.* **34** 11766
[41] Yao Q, Hu P, Sun P, Liu M, Dong R, Chao K, Liu Y, Jiang J and Jiang H 2020 *Adv. Mater.* **32** 1907888
[42] Samariha B and Rezaee Ebrahim Saraee K 2018 *Journal of Luminescence* **198** 389
[43] Hakami J, Kaynar Ü H, Ayvacikli M, Coban M B, Garcia-Guinea J, Townsend P D, Oglakci M and Can N 2022 *Ceramics International* **48** 32256
[44] Patel N P, Srinivas M, Modi D, Verma V and Murthy K V R 2018 *Rare Met.* **37** 587
[45] Murthy K V R, Prasad A S S and Rao M R 2012 *Physics Procedia* **29** 70
[46] Yin H, Li Y, Bai J, Ma M and Liu J 2017 *Journal of Materiomics* **3** 144
[47] Yuan H, Ma H, Wang G, Jia H and Sun X 2025 *Journal of Molecular Structure* **1321** 139776